

Multiple Quantum-Coherent Energy Transfer Pathways in Photosynthesis: Electronic-Vibrational Mixing within Photosystem II CP43/CP47 Antenna

Valentin Maffeis

Université Lyon, ENS Lyon, CNRS

Patricia Lorente

Consejo Superior de Investigaciones Científicas

Rafael Picorel

CSIC-Estación Experimental de Aula Dei, Avda. Montañana

Elisabet Romero (✉ eromero@iciq.es)

ICIQ <https://orcid.org/0000-0003-3630-1617>

Article

Keywords:

Posted Date: March 30th, 2022

DOI: <https://doi.org/10.21203/rs.3.rs-1506145/v1>

License:   This work is licensed under a Creative Commons Attribution 4.0 International License. [Read Full License](#)

Abstract

Photosynthesis, the biological process whereby the energy of the Sun is stored into biochemical energy, starts with energy absorption by light-harvesting complexes. These pigment-protein complexes are able to absorb and transfer energy with high speed and efficiency to the reaction center, the site of solar-energy conversion. To understand how these complexes work allows to elucidate strategies to design robust bio-inspired solar-energy conversion systems. Here, we report a two-dimensional electronic spectroscopy study of the photosystem II core antenna complexes, CP43 and CP47, and of monomeric chlorophyll *a* at cryogenic temperature aiming to investigate both the mechanism and the pathways of energy transfer with a focus on quantum-coherent phenomena. Our results demonstrate that multiple energy transfer pathways are active within CP43/CP47 and that electron-vibrational mixing promotes energy transfer via a vibronic-coherent mechanism. This work provides unprecedented detail on energy transfer within CP43/CP47 and contributes to our understanding of the natural light-harvesting design principles.

Introduction

In photosynthesis, the efficient solar-energy collection, transfer and conversion is accomplished by pigment-protein complexes, consisting of light-absorbing molecules (pigments) embedded into a protein matrix. During the early steps of photosynthesis, light-harvesting complexes absorb solar energy and transfer the resulting excitation energy to the reaction centre with remarkable speeds (10-100 ps timescale)¹ and with low energy losses². Once the energy reaches the reaction center, the excitation energy is converted into electrochemical energy by a series of electron transfer processes². In plants, the photosystem II (PSII) reaction center performs charge separation with near 100% efficiency² despite its highly disordered energy landscape. Hence, natural light-harvesting and reaction center complexes teaches us valuable lessons^{1,3} about how photo-excitation can be collected and directed using light-harvesting complexes and how this energy can be converted to a separation of charges, the energy conversion step required to convert sunlight into electricity or fuel.

Here we focus on the first steps of photosynthesis, that is, the energy transfer (ET) process in light-harvesting complexes. In photosystem II, the closest light-harvesting (or antenna) complexes to the reaction center are the CP43 and CP47 core antenna each containing 13 and 16 chlorophyll *a* (Chl) molecules, as well as 2 and 3 β -carotenes, respectively. Visual inspection of the X-ray structure⁴ reveals similar Chl arrangement for CP43/CP47 within the photosynthetic membrane with 8/8 Chl on the stromal side, 4/7 Chls on the luminal side, and one Chl located in between the stromal and luminal Chls. The electronic/vibrational properties and the ET dynamics within CP43/CP43 have been widely studied in the past by several steady-state and time-resolved spectroscopic techniques. It is worth noting the intrinsic complexity of interpreting the spectroscopic data for highly congested pigment-protein complex as CP43/CP47 where several absorption bands contribute to a narrow spectral window (from 650 to 700 nm, 1100 cm^{-1}). To overcome the spectral congestion problem and aid in the assignment of absorption bands to specific Chls within CP43/CP47, theoretical methods (structure-based modeling)⁵⁻⁷ arise as powerful tools. In summary, the main conclusions drawn from these experimental and theoretical comprehensive studies are: in CP43^{5,8-10}, the two lowest energy states at 77 K absorb at i) 682.5 nm with 3 nm (65 cm^{-1}) full-width at half maximum (fwhm) composed by two strongly coupled Chls close to the RC complex; and at ii) 680 nm with 11 nm (238 cm^{-1}) fwhm formed by six strongly

coupled Chls further from the RC; in CP47^{5,11,12}, at 77 K the two low-energy states absorb at i) 690 nm with 10 nm (220 cm^{-1}) fwhm corresponding to a single Chl far from the RC; and at ii) 683 nm with 8 nm (170 cm^{-1}) fwhm arising from three excitonically coupled Chls located closer to the RC than the 690 nm Chl. The investigation of the low-energy states is especially relevant since, after the absorbed excitation energy has reached the lowest energy states, they are responsible to transfer energy from CP43/CP47 to the RC complex, a process occurring on the 20-40 ps timescale¹³⁻¹⁶.

The ET dynamics within isolated CP43¹⁷⁻¹⁹ and CP47^{17,19} have been studied by time-resolved absorption (pump-probe) and fluorescence spectroscopy at 77 K and RT which yield similar ET rates: 200-400 fs and 2-3 ps at 77 K¹⁷, and 80-500 fs and 1-2 ps at RT^{18,19}. In addition, a slower 10-12 ps rate was observed in a visible/visible and visible/mid-infrared pump-probe study for CP43¹⁸ at RT, and a 17 ps energy relaxation was resolved only for CP47¹⁷ at 77 K. The combination of femtosecond transient absorption and picosecond transient fluorescence of CP43/CP47 at 77 K assisted with structure-based Monte Carlo simulations and energy transfer rates calculated by Foster theory concluded in the assignment of the experimentally observed multiphasic ET dynamics¹⁷: for both CP43/CP47 the 200-400 fs phase corresponds to relaxation to the lowest energy state within the Chls located on the stromal side (680 and 690 nm states for CP43 and CP47, respectively), and the slower 2-3 ps phase is associated with energy transfer from the luminal to the stromal side Chls. It is worth noting that the above-mentioned Monte Carlo simulations could not account for the narrow 682.5 nm CP43 state and, therefore, this state was not included in the interpretation of the ET dynamics.

With this contribution, our objective is to determine whether ET in CP43/CP47 proceeds via a quantum-coherent mechanism. In this manner we aim to shed light on the long-lasting debate^{20,21} about the presence and role of coherence in light-harvesting with confronting views both in favour²²⁻²⁷ and against^{28,29} the fact that non-trivial quantum coherent effects play a fundamental role in determining the speed and efficiency of ET. Furthermore, we revisit the ET process within CP43/CP47 to improve our understanding about the possible ET pathways in these biologically relevant light-harvesting complexes.

To achieve our goals, we have performed two-dimensional electronic spectroscopy (2DES) experiments at 77 K on CP43, CP47 and monomeric Chl. 2DES probes the evolution of an initially created coherent superposition of electronic/vibrational states excited by a spectrally broad laser pulse with high temporal and spectral resolution, and therefore, it provides great detail into the ET dynamics and coherences between the states excited. 2DES is advantageous with respect to the widely used transient absorption (pump-probe) spectroscopy because it delivers an additional data dimension; besides the detection axis (presented in pump-probe), 2DES also provides an excitation axis, it correlates excitation with emission events and hence, allows to visualize ET events and coherences between states in a direct manner. The cryogenic temperature (77 K) provides enhanced spectral resolution (with respect to RT) and avoids back-transfer reactions. Both effects facilitate the interpretation of the spectroscopic data and increase the amount of information that can be extracted which is especially relevant for spectrally congested complexes such as CP43/CP47. To aid in the interpretation of the complex 2DES data set and to provide an unambiguous assignment and interpretation of the spectral features, we have included the study of monomeric Chl where no Chl-Chl interactions are possible which allow us to compare the coherences present in isolated Chl molecules with the coherences observed

between the Chls in the CP43/CP47 pigment-protein complexes. Briefly, three types of quantum coherences can be observed in multi-chromophoric systems: electronic, mixed electronic-vibrational (vibronic), and vibrational^{3,30-32}. The electronic coherence between two states creates correlations between the wavefunctions of the states enabling the excitation energy to move rapidly and to coherently sample multiple pathways in space^{1,3,33-35}. Consequently, electronic coherence provides directionality³⁶, speed, robustness (low sensitivity to the intrinsic energetic disorder found in biological systems), and efficiency to energy transfer²²⁻²⁴ and electron transfer^{34,37-40} processes. The mixed electronic-vibrational coherence (so-called vibronic; that is, vibration-assisted electronic coherence) corresponds to electronic coherence promoted by an intra-molecular vibration of the system. In this case, whenever a vibration is in resonance with the energy gap between two electronic states involved in energy or electron transfer, the vibration mixes the electron-vibrational states^{41,42} and provides ultrafast and robust channels for energy and electron transfer processes. The vibrational coherence corresponds to coherence among the vibrational sublevels within ground and excited electronic states. In photosynthetic complexes, vibrational coherence is usually observed for vibrational frequencies that are higher in energy than the energy gaps between the electronic states. It is worth noting that for isolated Chl⁴³⁻⁴⁶ (or bacteriochlorophyll⁴⁷⁻⁵⁰) molecules in solution mainly vibrational coherences are observed.

Taking into account the electronic energy levels (absorbing from 650 to 700 nm, with energy differences up to 1100 cm^{-1}) and the vibrational frequencies (with several vibrational modes in the $100\text{-}1100\text{ cm}^{-1}$ range as observed by fluorescence line-narrowing (FLN) spectroscopy^{8,11}) present in CP43/CP47, we consider that the resonance between the vibrational modes and the energy gaps between the electronic states within the excitonic manifold is a reasonable possibility. Consequently, we anticipate that the vibration-assisted electronic coherent mechanism could be at play in the ET processes within CP43/CP47.

In this study, we investigate the ET pathways and mechanism within the PSII core CP43 and CP47 antenna complexes by applying 2DES to CP43, CP47 and Chl at 77 K. The correlation between excitation and emission events together with the high sensitivity of 2DES to the various types of coherences, allows us to disentangle multiple ET pathways within CP43/CP47, and to demonstrate that these ET processes occur via a vibronic quantum-coherent mechanism.

Results And Discussion

Two-dimensional electronic spectra: energy transfer dynamics

Two-dimensional electronic spectroscopy (2DES)³⁰⁻³² is a four-wave mixing spectroscopic technique capable of unravelling ultrafast energy transfer dynamics and the presence of coherences with high temporal and spectral resolution. The utilization of three broadband (90 nm fwhm centered at 695 nm, 2000 cm^{-1}) and ultrashort (15 fs) laser pulses allows to excite a coherent superposition of all the electronic and vibrational states covered by the laser spectrum (all the Chl Q_y absorption bands) (Fig. 1a) and to follow both the evolution of the initially created coherences and the ET processes. The first and second pulses create coherent superpositions of states, the third pulse induces the emission of a photon echo signal, and the fourth pulse interferes with the emitted signal to allow the measurement of both the amplitude and the phase of the signal. By sequentially delaying the first and second pulses by the coherence time (τ) for a fixed population time (T ,

time between the second and third pulses) and by Fourier transform along τ , the excitation dimension of the 2D spectrum is obtained whereas the detection axis is acquired by dispersing the photon echo signal for each τ in a spectrometer. Consequently, the 2D spectra correlates emission with excitation events as a function of T : the populations of the initially excited states appear on the diagonal [excitation wavelength (λ_{exc}) = detection wavelength (λ_{det})] as positive features representing ground state bleach (GSB) and stimulated emission (SE), the excited state absorption (ESA) appears as a negative band above diagonal, and ET processes are directly visualized as population transfer between a donor and an acceptor as below diagonal features (cross-peaks, CP). Furthermore, coherences between two states (A and B) are observed only at the CP positions (λ_A, λ_B) or (λ_B, λ_A) with their 2D signal amplitude oscillating as a function of T with a frequency corresponding to the difference in energy between the states involved ($\omega_A - \omega_B$)³⁰⁻³². The 2DES data has been collected with T from -1 ps to 1 ns, with the range between -104 to 2000 fs scanned with 8 fs steps to investigate whether the ultrafast ET processes occur via a coherent mechanism.

To assess the pathways and mechanism of ET in the PSII core antenna, we collected the 2D spectra of CP43, CP47, and monomeric Chl at 77 K. Figure 1a shows the linear absorption spectra of CP43, CP47 and Chl at 77 K together with the laser spectral profile utilized in the 2DES experiments. The laser light excites all the Q_y electronic states involved in ET and extends to the red side of the absorption spectra to allow the investigation of the low-lying energy states properties. The real rephasing 2D spectra for CP43, CP47 and Chl at 77 K are shown in Figure 1b for $T = 312$ fs after excitation, a population time at which, according to previously published transient absorption data¹⁷⁻¹⁹, the ultrafast phase of ET in CP43/CP47 is still in progress; hence, excited state population as well as energy transfer spectral features are present. Both the CP43/CP47 2D spectra show a rich diversity of spectral bands with diagonal and CP features whereas monomeric Chl shows a single band with the positive GSB and SE around the diagonal and the negative ESA above the diagonal, as expected for a monomeric molecule^{32,51,52}. For CP43 (Fig. 1b, Table 1), the diagonal band shows two maxima centered at ($\lambda_{excitation}, \lambda_{detection}$) (667.7,669.1) nm with an amplitude of 0.80, and (681.4,682.7) with an amplitude of 0.92 which correspond to the GSB and SE of the main bands present in the linear absorption spectrum at 669 and 682.5 nm. These central wavelengths are taken at the minima of the second derivative of the absorption spectrum which shows bands at 682.5, 677.5 (weak), 669, and 660.5 nm. In the following, we will use the notation [$(\lambda_{excitation}, \lambda_{detection})$ nm, *amplitude*] to describe the spectral features (note that all 2D spectra has been normalized to one at the maximum of the 2D amplitude at $T = 104$ fs.) (Table 1). Below diagonal, three CPs are readily visible at [(675.4,682.7) nm, 0.45], [(669.2,682.7) nm, 0.42], and [(664.5,682.2) nm, 0.38]. These CPs are signatures of ET and/or coherences between the 664.5, 669.2, and 675.4 nm states and the low-energy 682.5 nm state. Note that all these states are present in the absorption spectrum yet the exact band position differs from absorption to 2DES data due to band overlap. For CP47 (Fig. 1b, Table 2), one maximum [(675.8,676.6) nm, 0.73] and two shoulders at [(681.4,682.7) nm, 0.60] and [(670.3,670.5) nm, 0.60] are distinguishable on the diagonal corresponding to the GSB and SE of the 683, 676.5 and 671 nm bands observed in the linear absorption spectrum (an additional band appears in the second derivative of the absorption at 660.5 nm). In this case, due to stronger spectral overlap (with respect to CP43) the CPs are not as well-resolved as in CP43, yet in CP47 the CPs are also clearly visible below diagonal along two detection wavelengths: 676 and 683 nm (see Fig. 2b for better resolved CPs at longer T). These CPs point towards the presence of ET and/or coherences among the 683, 676.5 and 671 nm states.

Table 1. CP43 real rephrasing 2D spectral features

<i>T</i>	Diagonal ₆₈₂	Diagonal ₆₆₉	CP ₆₇₅₋₆₈₂	CP ₆₆₉₋₆₈₂	CP ₆₆₅₋₆₈₂	CP ₆₅₉₋₆₈₂	CP ₆₅₄₋₆₈₂
112 fs	681.1,682.2 1.00	667.7,669.1 1.00	675.1,682.2 0.49 155 cm ⁻¹	669.5,682.2 0.37 280 cm ⁻¹	664.8,682.2 0.26 385 cm ⁻¹	659.1,681.8 0.14 505 cm ⁻¹	653.9,681.3 0.08 615 cm ⁻¹
312 fs	681.4,682.7 0.92	667.7,669.1 0.80	675.4,682.2 0.47 150 cm ⁻¹	669.5,682.7 0.39 295 cm ⁻¹	664.5,682.2 0.34 390 cm ⁻¹	659.1,681.8 0.21 505 cm ⁻¹	653.9,681.3 0.13 615 cm ⁻¹
496 fs	681.4,682.7 0.90	667.7,669.1 0.67	675.4,682.7 0.45 160 cm ⁻¹	669.2,682.7 0.42 295 cm ⁻¹	664.5,682.2 0.38 390 cm ⁻¹	659.1,681.8 0.25 505 cm ⁻¹	653.9,681.3 0.15 615 cm ⁻¹
992 fs	681.8,683.2 0.88	667.7,668.7 0.46	675.8,683.2 0.42 160 cm ⁻¹	669.2,682.7 0.45 295 cm ⁻¹	664.8,682.2 0.44 385 cm ⁻¹	659.1,681.8 0.31 505 cm ⁻¹	653.9,681.3 0.17 615 cm ⁻¹
10 ps	681.8,683.7 0.60	666.6,667.8 0.11	675.8,683.7 0.29 245 cm ⁻¹	666.6,683.2 0.53 365 cm ⁻¹		659.1,681.7 0.37 515 cm ⁻¹	653.9,681.3 0.24 615 cm ⁻¹

The excitation and detection wavelengths are given in nm separated by a comma (excitation,detection). The features for which the maximum precise position could not be determined are indicated in grey. In these cases, the position was chosen based on the nearby diagonal and CP positions. The amplitude of each feature is displayed below its position. The energy difference between all CPs is indicated in cm⁻¹.

Table 2. CP47 real rephrasing 2D spectral features

<i>T</i>	Diagonal ₆₈₃	Diagonal ₆₇₆	Diagonal ₆₇₀	CP ₆₇₆₋₆₈₃	CP ₆₇₀₋₆₈₃	CP ₆₆₅₋₆₈₃	CP ₆₇₀₋₆₇₆	CP ₆₆₅₋₆₇₆
112 fs	681.4,682.7 0.66	675.8,676.6 0.93	670.0,670.0 0.92	675.8,682.7 0.40 150 cm ⁻¹	671.7,682.7 0.29 240 cm ⁻¹	667.0,682.7 0.18 345 cm ⁻¹	670.0,676.1 0.50 135 cm ⁻¹	662.3,676.1 0.22 310 cm ⁻¹
312 fs	681.4,682.7 0.60	675.8,676.6 0.73	670.3,670.5 0.60	675.8,682.7 0.33 150 cm ⁻¹	671.7,682.7 0.27 240 cm ⁻¹	667.0,682.2 0.21 335 cm ⁻¹	670.0,676.1 0.38 135 cm ⁻¹	662.3,676.1 0.22 310 cm ⁻¹
496 fs	681.8,682.7 0.48	675.8,676.1 0.56	670.3,670.5 0.50	675.8,682.7 0.28 150 cm ⁻¹	671.7,682.7 0.26 240 cm ⁻¹	667.0,682.7 0.22 345 cm ⁻¹	670.0,676.1 0.30 135 cm ⁻¹	662.3,676.1 0.20 310 cm ⁻¹
2.5 ps	683.0,684.1 0.35	676.2,676.6 0.33	669.2,669.6 0.27	676.9,684.1 0.25 155 cm ⁻¹	670.3,683.7 0.26 295 cm ⁻¹	662.3,682.2 0.20 440 cm ⁻¹	669.2,676.1 0.19 150 cm ⁻¹	662.3,676.1 0.16 310 cm ⁻¹
20 ps	683.0,684.1 0.18	675.1,675.6 0.13	669.5,670.1 0.14	675.4,684.6 0.15 200 cm ⁻¹	670.3,683.7 0.17 295 cm ⁻¹	662.3,682.2 0.14 440 cm ⁻¹	668.1,675.6 0.08 165 cm ⁻¹	663.0,676.1 0.08 290 cm ⁻¹

The excitation and detection wavelengths are given in nm separated by a comma (excitation,detection). The features for which the maximum precise position could not be determined are indicated in grey. In these cases, the position was chosen based on the nearby diagonal and CP positions. The amplitude of each feature is displayed below its position. The energy difference between all CPs is indicated in cm⁻¹.

Remarkably, the application of 2DES at 77 K allows the observation of well-resolved diagonal and CP spectral features that remain hidden when employing other spectroscopic methods such as transient absorption. Here, the additional detection dimension of the 2DES data allows us to directly visualize ET processes between closely spaced electronic states, with energy differences as low as 135 cm⁻¹. After identifying the main spectral

features in the 2D spectra, we analyze the ET dynamics. Figure 2a/b shows the CP43/CP47 real rephasing 2D spectra at four representative T (112 fs, 496 fs, 1 ps, 10 ps)/ (112 fs, 496 fs, 2.5 ps, 20 ps). The 2D spectra for monomeric Chl as a function of T is not shown because, as expected, no significant spectral evolution is observed⁴³⁻⁴⁶ but only the partial decay of the GSB, SE and ESA in the time scale of our experiment (the longest probed T is 1 ns). At $T = 0$ fs, coherence is the only origin of CPs since no ET can occur right upon excitation. Yet, strong coherent artefacts that cannot be eliminated are present until $T \approx 100$ fs due to the wave-mixing nature of 2DES³², resulting in $T = 104$ fs being the first T free from artefacts in our datasets. As the system evolves over time, the coherence usually disappears through intramolecular and intermolecular (mostly pigment-environment) interactions³².

The position and amplitude of the main diagonal and CP features for CP43/CP47 at five representative T are summarized in Table 1 and Table 2, respectively (note that the features that appear as shoulders not as maxima are shown in grey). In addition, the difference in energy between the states involved in each CP is indicated. For CP43 (Fig. 2a, Table 1), two diagonal maxima are observed at 682 and 669 nm, together with five CPs connecting the states absorbing at 675, 669, 665, 659 and 654 nm with the low-lying 682.5 nm state. It is worth noting that even though the $CP_{659-682}$ and the $CP_{654-682}$ do not appear as separated CPs along the excitation axis due to band overlap, they do emerge as maxima along the detection axis. The overall spectral evolution consists of (from 112 to 992 fs): the *fast* decay of the $Diagonal_{669}$ amplitude (from 1.00 to 0.46), the *slow* decay of the $Diagonal_{682}$ amplitude (from 1.00 to 0.88), the moderate decrease of the $CP_{675-682}$ (from 0.49 to 0.42) and the increase of the other CPs: $CP_{669-682}$ (from 0.37 to 0.45), $CP_{665-682}$ (from 0.26 to 0.44), $CP_{659-682}$ (from 0.14 to 0.31), and $CP_{654-682}$ (from 0.08 to 0.17). The evolution of the spectral features reveals ET from the 675, 669, 665, 659, and 654 nm states to the 682.5 nm state. The $Diagonal_{669}$ band decays into the $Diagonal_{682}$ feature via the $CP_{669-682}$: the $Diagonal_{669}$ amplitude decreases while the $CP_{669-682}$ amplitude increases due to population transfer to the 682.5 nm state. At the same time, the $Diagonal_{682}$ amplitude should increase, yet it decays slightly (from 1.00 to 0.88). This could be explained by that fact that two states contribute to the $Diagonal_{682}$: the broad [680 nm (11 nm fwhm)] and the narrow [682.5 (3 nm fwhm)] low-energy states since both are excited by the laser pulses. In this case, it is reasonable to consider that the decay of the 680 nm state GSB and SE hinders the observation of the increase of the $Diagonal_{682}$ amplitude due to energy transfer from the 669 nm to the 682.5 nm state (see below). Furthermore, and even though the $Diagonal_{675}$ and the $Diagonal_{665}$ are not resolved as separated bands due to spectral overlap, the presence of the $CP_{675-682}$ and the $CP_{665-682}$ implies that ET from both the 665 and the 675 nm states to the 682.5 nm state occurs on an sub-picosecond time scale (the moderate decrease, instead of increase, of the $CP_{675-682}$ is most likely caused by band overlap with the $Diagonal_{682}$ band that decays slightly in the same time scale). Moreover, the high sensitivity of 2DES allows us to visualize ET from higher energy states (absorbing at 659 and 654 nm) via the presence of the $CP_{659-682}$ and $CP_{654-682}$. At longer times, $T = 10$ ps, the $Diagonal_{669}$ feature has disappeared almost completely (amplitude 0.11), while the $Diagonal_{682}$ is clearly visible (amplitude 0.60) an indication that this state has been populated by ET from higher-energy states.

Remarkably, the ET from the 665, 669 and 675 nm states to the narrow (3 nm fwhm) low-energy 682.5 nm state is revealed by two facts: the CPs central wavelength (682.5 nm) and their width (around 3 nm). It is worth noting that even though the $Diagonal_{682}$ is broad (at least 10 nm) owing to the population of both broad and

narrow low-energy states [680 nm (11 nm fwhm) and 682.5 (3 nm fwhm)] by the laser excitation, the fact that the CPs are as narrow as the 682.5 nm state and centered at the same wavelength demonstrates that only this state receives excitation energy from higher energy states. The observation of three well-resolved CPs reveals the existence of, at least, three distinct ET pathways from the different Chls pools absorbing around 675, 669 and 665 nm to the 682.5 nm state, whereas the broad low-energy 680 nm state does not receive energy (i.e., remains unconnected) from the high-energy states.

For CP47 (Fig. 2b, Table 2), the overall spectral evolution is similar to CP43 yet with significant differences. In this case, due to stronger spectral overlap half of the spectral features displayed in Table 2 do not appear as separated maxima; therefore, and in order to analyze their amplitudes, their positions have been taken from better-resolved 2D spectra (for instance at $T = 496$ fs for the CPs present along the 683 nm detection wavelength at and $T = 2.5$ ps for the CPs along the 676 nm detection wavelength). At $T = 112$ fs, the GSB and SE features have maximum amplitude (≈ 0.94) between 667 and 677 nm along the diagonal and extend to the red up to around 685 nm with half the maximum amplitude (≈ 0.47). The CPs start to be apparent below diagonal along the detection axis around 676 and 683 nm although to a lower extent than for CP43. At longer T , 496 fs and 2.5 ps, the CPs are better resolved and clearly visible. In fact, at these population times CP47 displays two kinds of CPs, three CPs connecting the 676, 670, and 665 nm states ($CP_{676-683}$, $CP_{670-683}$, and $CP_{665-683}$) with the low-energy 683 nm state (similar to CP43); and two CPs relating the 670 and 665 nm states ($CP_{670-676}$ and $CP_{665-676}$) with the 676 nm state. The latter CPs appear as separated bands at 2.5 ps. At longer times, $T = 20$ ps, three diagonal features are visible at 683, 676 and 670 nm; and most of the CPs emerge as maxima. Unfortunately, in this case the strong band overlap complicates the analysis of the 2D spectral features amplitude, which in almost all cases decreases as function of time, most likely due to pigment-environment interactions³².

Nevertheless, and despite the strong spectral congestion, the CP47 spectral features demonstrate the presence of multiple ET pathways with various donor and acceptor states: the lowest-energy state (683 nm) receives energy from higher-energy states (676, 670, and 665 nm), the high-energy states (670 and 665 nm) transfer energy to the 676 nm state, and the 676 nm state receives and transfers energy.

Two-dimensional frequency maps: coherences between states involved in ET

After analyzing the ET dynamics, now we explore whether ET in CP43/CP47 proceeds via a coherent mechanism. As it was previously indicated, coherence between two states (A and B) emerges in the real rephasing 2D spectra as a CP [(λ_A, λ_B) or (λ_B, λ_A)] which signal amplitude oscillates as a function of T with a frequency equivalent to the difference in energy between the states ($\omega_A - \omega_B$)³⁰⁻³². To examine the presence of coherent ET in CP43/CP47, the quantum beats (2D signal amplitude oscillations as a function of T) have been isolated from the 2D traces by subtracting the ET dynamics (applying and subtracting a polynomial fit to the traces) and analyzed by Fourier transform (FT) in order to retrieve the oscillation frequencies present in the datasets (CP43/CP47 and Chl). The FT has been performed on the traces from 104 to 1504 fs which yields a 40 cm^{-1} frequency resolution ($\pm 20 \text{ cm}^{-1}$) with the maximum sampled frequency being $\approx 2100 \text{ cm}^{-1}$ (8 fs step employed within the FT range). Figure 3 shows the results of the FT analysis up to 850 cm^{-1} . Plotting the

maximum amplitude of each frequency found in the complete 2D dataset for each studied system (Fig. 3a) provides a general view of the dominant frequencies present in the data. Yet, a detailed physical picture is obtained by analyzing the 2D frequency maps (Fig. 3b, c, and d). Differently from the 2D spectra which contain contributions from all absorbing and emitting states, the frequency maps display only the states which oscillate at a specific frequency, hence these maps reveal coherences between electronic/vibrational states. The major frequencies for CP43 are ($\pm 20 \text{ cm}^{-1}$): 150, 265, 300, 345, 400, 520, and 750 cm^{-1} (Fig. 3b) (the 2D frequency maps for 300, 400, and 520 cm^{-1} are shown in the Supplementary Fig. S1). For CP47 the dominant frequencies are ($\pm 20 \text{ cm}^{-1}$): 130, 265, 300, 345, and 740 cm^{-1} (Fig. 3c) (the 2D frequency maps for 300 cm^{-1} is shown in the Supplementary Fig. S1). In the case of Chl, the observed frequencies related to the ones found for CP43/CP47 are ($\pm 20 \text{ cm}^{-1}$): 170, 265, 305, 345, 395, 520 and 740 cm^{-1} (Fig. 3d) (the 2D frequency maps for 305, 395, and 520 cm^{-1} are shown in the Supplementary Fig. S1). It is interesting to note that for the three samples almost all frequencies retrieved by FT of the 2DES data have been previously observed in their FLN spectra (except for the frequencies below 250 cm^{-1} in CP43/CP47 that overlap with the strong phonon wing in FLN) (CP43⁸, CP47¹¹, and Chl⁵³). Since the CP43/CP47 oscillation frequencies have their counterparts in the FLN spectrum of isolated Chl, we can conclude that the frequencies observed in 2DES correspond to Chl intramolecular vibrations. The information about the coherences present in the 2D frequency maps can be understood as follows. Electronic and vibronic coherence between two states (A and B) appears as a CP $[(\lambda_A, \lambda_B) \text{ or } (\lambda_B, \lambda_A)]$ in the 2D frequency map corresponding the difference in energy between the states ($\omega_A - \omega_B$)³⁰⁻³². For vibrational coherence the chair-type structure emerges^{3,32,34,44,45} in the real rephasing 2D frequency maps as a combination of vibrational coherence generated via the GSB and SE [see Fig.3d (Chl 740 cm^{-1} map) for an example], whereas the vibrational coherence generated only via the SE emerges with the amplitude distribution of the Chl maps at 265 and 345 cm^{-1} (Fig.3d) where the CP below the diagonal feature is absent³².

The interpretation of the 2D frequency maps (Fig. 3b, c, and d) is assisted by: i) the calculation of the energy difference between the electronic states involved in each ET step (states connected by CPs) (Table 1/2 for CP43/CP47), ii) the indication of the electronic states center wavelength as horizontal and vertical back dotted lines, iii) the inclusion of the below and above diagonal lines shifted by the frequency of each map as thin black lines.

For CP43 (Fig. 3b), the low frequency 150 cm^{-1} map corresponding to the CP₆₇₅₋₆₈₂ displays minor but visible amplitude at the CP position, indicating that ET from the 675 to the 682 nm state may proceed via a vibronic coherent mechanism. The related monomeric Chl map at 170 cm^{-1} clearly deviates from the chair-type structure and from the structure observed for CP43/CP47, still, a virtually identical 2D map was observed recently for monomeric bacteriochlorophyll *a* at 77 K⁵⁰ (in isopropanol as used here). The 265 cm^{-1} map which corresponds to the CP₆₆₉₋₆₈₂ displays a complicated amplitude distribution. In this case, it is extremely useful to compare the CP43 map with the related Chl map which shows the amplitude distribution of the vibrational coherence generated via SE³². In fact, the CP43 map resembles the Chl map, it contains the above diagonal, the diagonal and the two below diagonal features as the Chl map yet with a significant difference: the intense CP₆₆₉₋₆₈₂ feature. Consequently, we conclude that for CP43 the 265 cm^{-1} map represents both vibrational and vibronic coherence, the latter indicating that ET from the 669 to the 682 nm state occurs via a coherent

mechanism. The 345 cm^{-1} map ($\text{CP}_{665-682}$) shows a dominant signal at the CP position both below and above diagonal (note that the above diagonal CP feature is not exactly at the $\text{CP}_{682-665}$ position most likely due to spectral overlap with the ESA signal), with a minor contribution from the vibrational coherence via SE, indicating the presence of vibronic coherence between the 665 to the 682 nm state which implies that this ET channel also exploits the advantages of coherence. The 750 cm^{-1} map reveal the chair-type structure corresponding to purely vibrational coherence, that is, this vibration is too high in energy to couple to the electronic energy gaps. For CP47 (Fig. 3c), the 130 cm^{-1} map corresponds to the CPs connecting the 676 and the 683 nm states ($\text{CP}_{676-683}$) as well as the 670 and the 676 nm states ($\text{CP}_{670-676}$). The map shows a clear feature at the $\text{CP}_{676-683}$ position, indicating that ET between these states occurs via a coherent mechanism. In addition, the CP feature extends to the $\text{CP}_{670-676}$ suggesting that also these two states might be connected by coherent ET. The 265 cm^{-1} frequency is close in energy to the energy gaps between the 670 and 683 nm states as well as between the 665 and 676 nm states ($\text{CP}_{670-683}$ and $\text{CP}_{665-676}$, respectively), and indeed, both CPs appear in the 265 cm^{-1} frequency map with significant amplitude. Again, the shape of the amplitude distribution in the frequency map strongly indicates that ET between the states involved in the above-mentioned CPs proceeds via a coherent mechanism. The 345 cm^{-1} map ($\text{CP}_{665-683}$) displays intense amplitude features both below and above diagonal at the CP position. Similarly to CP43, the minor participation of vibrational coherence contributes to the diagonal and above diagonal CP and the overlap with the ESA band may shift the possible vibronic above diagonal feature slightly to the blue. In any case, the strong signal at the $\text{CP}_{665-683}$ position provides compelling evidence of coherent ET from the 665 to the 683 nm state. The 740 cm^{-1} map display the chair-type amplitude shape consistent with purely vibrational coherence, therefore, we conclude that this high energy vibration is not able to couple to the electronic energy gaps.

Concluding Remarks

The application of 2DES at 77 K to study the ET dynamics and mechanism in the PSII core antenna CP43 and CP47, and the comparison with the coherences present in monomeric Chl, has allowed us to disentangle, for the very first time, the ET pathways within CP43/CP47 with unprecedented detail. For CP43, all the high-energy states (absorbing at 675, 669 and 665 nm) transfer energy directly to the narrow low-energy state absorbing at 682.5 nm; whereas for CP47, the high-energy states (absorbing at 667 and 670 nm) transfer energy to lower-energy states (absorbing at 676 and 683 nm), the lowest-energy state (absorbing at 683 nm) can receive energy from three higher-energy states (absorbing at 667, 670 and 676 nm), and the medium-energy state (absorbing at 676 nm) is capable of both receiving and transferring energy from the 667 and 670 nm states and to the 683 nm state, respectively. Remarkably, in both CP43/CP47 the lowest-energy transitions (at 682.5 nm in CP43 and at 683 nm in CP47) are associated with strongly coupled Chls located close to the $\text{RC}^{5,17}$, position which makes them the most optimal candidates to receive energy from the higher-energy states to ensure the subsequent transfer of energy to the reaction center.

Regarding the mechanism of ET, with this contribution we have been able to shed light into the long-lasting discussion about the presence of coherent ET in light-harvesting systems. We consider that the results and analysis presented here demonstrate that ET in CP43 and CP47 pigment-protein complexes proceeds via a quantum-coherent mechanism. The electronic-vibrational mixing between the electronic states involved in all

the observed ET pathways and the intra-molecular vibrations visualized in the 2D frequency maps as clear vibronic coherence features, provide convincing experimental evidence to support our conclusion.

We envision that our findings will pave the way to implement quantum-coherent ET in artificial light-harvesting complexes to develop robust, fast and efficient solar-energy conversion systems.

Methods

Sample preparation

Isolated CP43 and CP47 were prepared from spinach as previously described⁵⁴. The CP43 (CP47) samples were diluted in a buffer containing 50 (20) mM Bis-Tris pH 7.8 (6), 0.09% β -DM (w/v), and 60% glycerol to an optical density of ≈ 0.3 in 500 μm at the Q_Y maximum. Chlorophyll *a* isolated from spinach in powder form was dissolved in isopropanol to an optical density of ≈ 0.3 in 500 μm at the Q_Y maximum. All experiments were performed in a liquid nitrogen cryostat (OptistatDN2, Oxford Instruments).

2DES experimental setup and data acquisition

2D spectra was measured in a diffractive optic-based inherently phase-stabilized four-wave mixing setup in the BOXCARS configuration with double modulation lock-in detection for additional noise reduction and enhanced sensitivity. The laser system (PHAROS, Light Conversion) repetition rate was 1 kHz. The laser pulses generated by a home-built non-collinear optical parametric amplifier were centered at 695 nm (95 nm fwhm) and had 15 fs pulse duration. The 2DES experiments were collected at 5 and 12 nJ/pulse. The data presented here was taken with 12nJ/pulse, an excitation intensity free of annihilation effects (as indicated by power dependence studies). The coherence time (τ) was scanned in 1 fs steps from -150 to 280 fs, from -110 to 300 fs, and from -110 to 280 fs for CP43, CP47 and Chl, respectively. The population time (T) was scanned from -104 to 2000 fs in 8 fs steps, from 2 ps to 5 ps in 100 fs steps, and from 5 ps to 10 ps in 500 fs steps. Additional 2D spectra were collected at longer T (-1, 15, 20, 25, 30, 50, 100, 250, 500, 750 ps and 1 ns).

Declarations

Data Availability

The authors declare that the data supporting the findings of this study are available within the paper (and its supplementary information files). All data are available from the authors upon reasonable request.

Acknowledgements

VM was supported by the European Union's Horizon 2020 research and innovation program under the Marie Skłodowska-Curie programme (grant agreement No. 754510). ER acknowledges the support from the European Research Council under the ERC starting grant [Grant agreement No. 805524 (BioInspired_SolarH2)] and the Agencia Estatal de Investigación and the Spanish Ministry for Science and Innovation for financial support in

the framework of the Severo-Ochoa excellence initiative (project reference CEX2019-000925-S-20-5). P.L. and R.P. thank PN (project reference RTI2018-097755-B-100) and DGA (project reference A09-20R).

Authors contributions

E.R. conceived the research. P.L. and R.P. prepared the CP43 and CP47 samples. V.M. performed the experiments. V.M. and E.R. analyzed the experimental data and wrote the manuscript. All authors discussed the results and contributed to the manuscript.

Competing financial interests

The authors declare no competing financial interests.

Materials & Correspondence

Correspondence and requests for materials should be addressed to E.R.

References

1. Scholes, G. D., Fleming, G. R., Olaya-Castro, A. & van Grondelle, R. Lessons from nature about solar light harvesting. *Nat. Chem.* **3**, 763–774 (2011).
2. Blankenship, R. E. *Molecular Mechanisms Of Photosynthesis*. (Blackwell Science Ltd, Oxford, 2002).
3. Romero, E., Novoderezhkin, V. I. & van Grondelle, R. Quantum design of photosynthesis for bio-inspired solar-energy conversion. *Nature* **543**, 355–365 (2017).
4. Umena, Y., Kawakami, K., Shen, J.-R. & Kamiya, N. Crystal structure of oxygen-evolving photosystem II at a resolution of 1.9 Å. *Nature* **473**, 55–60 (2011).
5. Raszewski, G. & Renger, T. Light Harvesting in Photosystem II Core Complexes Is Limited by the Transfer to the Trap: Can the Core Complex Turn into a Photoprotective Mode? *J. Am. Chem. Soc.* **130**, 4431–4446, doi:10.1021/ja7099826 (2008).
6. Müh, F., Madjet, M. E.-A. & Renger, T. Structure-based simulation of linear optical spectra of the CP43 core antenna of photosystem II. *Photosyn. Res.* **111**, 87–101, doi:10.1007/s11120-011-9675-8 (2012).
7. Müh, F. *et al.* The quest for energy traps in the CP43 antenna of photosystem II. *J. Photoch. Photobio. B* **152**, 286–300, doi:https://doi.org/10.1016/j.jphotobiol.2015.05.023 (2015).
8. Groot, M.-L. *et al.* Spectroscopic properties of the CP43 core antenna protein of photosystem II. *Biophys. J.* **77**, 3328–3340 (1999).
9. Jankowiak, R. *et al.* The CP43 Core Antenna Complex of Photosystem II Possesses Two Quasi-Degenerate and Weakly Coupled Qy-Trap States. *J. Phys. Chem. B* **104**, 11805–11815, doi:10.1021/jp0025431 (2000).

10. Hall, J., Renger, T., Picorel, R. & Krausz, E. Circularly polarized luminescence spectroscopy reveals low-energy excited states and dynamic localization of vibronic transitions in CP43. *Biochim. Biophys. Acta* **1857**, 115–128, doi:<https://doi.org/10.1016/j.bbabi.2015.09.012> (2016).
11. de Weerd, F. L., Palacios, M. A., Andrizhiyevskaya, E. G., Dekker, J. P. & van Grondelle, R. Identifying the lowest electronic states of the chlorophylls in the CP47 core antenna protein of photosystem II. *Biochemistry* **41**, 15224–15233 (2002).
12. Hall, J., Renger, T., Müh, F., Picorel, R. & Krausz, E. The lowest-energy chlorophyll of photosystem II is adjacent to the peripheral antenna: Emitting states of CP47 assigned via circularly polarized luminescence. *Biochim. Biophys. Acta* **1857**, 1580–1593, doi:<https://doi.org/10.1016/j.bbabi.2016.06.007> (2016).
13. Andrizhiyevskaya, E. G., Frolov, D., van Grondelle, R. & Dekker, J. P. On the role of the CP47 core antenna in the energy transfer and trapping dynamics of Photosystem II. *Phys. Chem. Chem. Phys.* **6**, 4810–4819, doi:10.1039/b411977k (2004).
14. Broess, K. *et al.* Excitation energy transfer and charge separation in photosystem II membranes revisited. *Biophys. J.* **91**, 3776–3786, doi:10.1529/biophysj.106.085068 (2006).
15. Pan, J. *et al.* Ultrafast energy transfer within the photosystem II core complex. *Phys. Chem. Chem. Phys.* **19**, 15356–15367, doi:10.1039/c7cp01673e (2017).
16. Shibata, Y., Nishi, S., Kawakami, K., Shen, J.-R. & Renger, T. Photosystem II does not possess a simple excitation energy funnel: time-resolved fluorescence spectroscopy meets theory. *J. Am. Chem. Soc.* **135**, 6903–6914, doi:10.1021/ja312586p (2013).
17. de Weerd, F. L., van Stokkum, I. H. M., van Amerongen, H., Dekker, J. P. & van Grondelle, R. Pathways for Energy Transfer in the Core Light-Harvesting Complexes CP43 and CP47 of Photosystem II. *Biophys. J.* **82**, 1586–1597, doi:[https://doi.org/10.1016/S0006-3495\(02\)75510-0](https://doi.org/10.1016/S0006-3495(02)75510-0) (2002).
18. Di Donato, M., van Grondelle, R., van Stokkum, I. H. M. & Groot, M. L. Excitation Energy Transfer in the Photosystem II Core Antenna Complex CP43 Studied by Femtosecond Visible/Visible and Visible/Mid-Infrared Pump Probe Spectroscopy. *J. Phys. Chem. B* **111**, 7345–7352, doi:10.1021/jp068315+ (2007).
19. Casazza, A. P., Szczepaniak, M., Müller, M. G., Zucchelli, G. & Holzwarth, A. R. Energy transfer processes in the isolated core antenna complexes CP43 and CP47 of photosystem II. *BBA-Bioenergetics* **1797**, 1606–1616, doi:<https://doi.org/10.1016/j.bbabi.2010.05.008> (2010).
20. Ball, P. *Is photosynthesis quantum-ish?*, <<https://physicsworld.com/a/is-photosynthesis-quantum-ish/>> (2018).
21. Ball, P. The dawn of quantum biology. *Nature* **474**, 272–274 (2011).
22. Higgins, J. S. *et al.* Photosynthesis tunes quantum-mechanical mixing of electronic and vibrational states to steer exciton energy transfer. *Proc. Natl. Acad. Sci. U.S.A.* **118**, e2018240118, doi:10.1073/pnas.2018240118 (2021).
23. Higgins, J. S. *et al.* Redox conditions correlated with vibronic coupling modulate quantum beats in photosynthetic pigment–protein complexes. *Proc. Natl. Acad. Sci. U.S.A.* **118**, e2112817118, doi:10.1073/pnas.2112817118 (2021).
24. Singh, D. Coherent Speedup of Excitation Energy Transfer in PC645. *J. Phys. Chem. B* **125**, 557–561, doi:10.1021/acs.jpcc.0c10719 (2021).

25. Kim, J. *et al.* Vibrational Modes Promoting Exciton Relaxation in the B850 Band of LH2. *J. Phys. Chem. Lett.*, 1099–1106, doi:10.1021/acs.jpcllett.1c03868 (2022).
26. Kim, J. *et al.* Low-Frequency Vibronic Mixing Modulates the Excitation Energy Flow in Bacterial Light-Harvesting Complex II. *J. Phys. Chem. Lett.* **12**, 6292–6298, doi:10.1021/acs.jpcllett.1c01782 (2021).
27. Zhu, R. *et al.* Vibrational and vibronic coherences in the energy transfer process of light-harvesting complex II revealed by two-dimensional electronic spectroscopy. *J. Chem. Phys.* **156**, 125101, doi:10.1063/5.0082280 (2022).
28. Duan, H.-G. *et al.* Nature does not rely on long-lived electronic quantum coherence for photosynthetic energy transfer. *Proc. Natl. Acad. Sci. U.S.A.* **114**, 8493–8498, doi:10.1073/pnas.1702261114 (2017).
29. Cao, J. *et al.* Quantum biology revisited. *Sci. Adv.* **6**, eaaz4888 (2020).
30. Schlau-Cohen, G. S., Dawlaty, J. M. & Fleming, G. R. Ultrafast multidimensional spectroscopy: Principles and applications to photosynthetic systems. *IEEE J. Sel. Topics Quantum Electron.* **18**, 283–295 (2012).
31. Collini, E. Spectroscopic signatures of quantum-coherent energy transfer. *Chem. Soc. Rev.* **42**, 4932–4947 (2013).
32. Biswas, S., Kim, J., Zhang, X. & Scholes, G. D. Coherent two-dimensional and broadband electronic spectroscopies. *Chem. Rev.* **122**, 4257–4321, doi:10.1021/acs.chemrev.1c00623 (2022).
33. Scholes, G. D. *et al.* Using coherence to enhance function in chemical and biophysical systems. *Nature* **543**, 647–656, doi:10.1038/nature21425 (2017).
34. Romero, E. *et al.* Quantum coherence in photosynthesis for efficient solar-energy conversion. *Nat. Phys.* **10**, 676–682 (2014).
35. Cheng, Y. C. & Fleming, G. R. Dynamics of light harvesting in photosynthesis. *Annu. Rev. Phys. Chem.* **60**, 241–262 (2009).
36. Ishizaki, A. & Fleming, G. R. Theoretical examination of quantum coherence in a photosynthetic system at physiological temperature. *Proc. Natl. Acad. Sci. U. S. A.* **106**, 17255–17260 (2009).
37. Fuller, F. D. *et al.* Vibronic coherence in oxygenic photosynthesis. *Nat. Chem.* **6**, 706–711 (2014).
38. Ma, F. *et al.* Dynamics of diverse coherences in primary charge separation of bacterial reaction center at 77 K revealed by wavelet analysis. *Photosynth Res*, doi:10.1007/s11120-021-00881-9 (2021).
39. Ma, F., Romero, E., Jones, M. R., Novoderezhkin, V. I. & van Grondelle, R. Vibronic Coherence in the Charge Separation Process of the Rhodobacter sphaeroides Reaction Center. *J. Phys. Chem. Lett.* **9**, 1827–1832, doi:10.1021/acs.jpcllett.8b00108 (2018).
40. Ma, F., Romero, E., Jones, M. R., Novoderezhkin, V. I. & van Grondelle, R. Both electronic and vibrational coherences are involved in primary electron transfer in bacterial reaction center. *Nat. Comm.* **10**, 933, doi:10.1038/s41467-019-08751-8 (2019).
41. Novoderezhkin, V. I., Romero, E., Prior, J. & van Grondelle, R. Exciton-vibrational resonance and dynamics of charge separation in the photosystem II reaction center. *Phys. Chem. Chem. Phys.* **19**, 5195–5208, doi:10.1039/c6cp07308e (2017).
42. Novoderezhkin, V. I., Romero, E. & van Grondelle, R. How exciton-vibrational coherences control charge separation in the photosystem II reaction center. *Phys. Chem. Chem. Phys.* **17**, 30828–30841 (2015).

43. Du, J., Teramoto, T., Nakata, K., Tokunaga, E. & Kobayashi, T. Real-time vibrational dynamics in chlorophyll *a* studied with a few-cycle pulse laser. *Biophysical Journal* **101**, 995–1003, doi:10.1016/j.bpj.2011.07.011 (2011).
44. Moca, R., Meech, S. R. & Heisler, I. A. Two-dimensional electronic spectroscopy of chlorophyll *a*: solvent dependent spectral evolution. *J. Phys. Chem. B* **119**, 8623–8630, doi:10.1021/acs.jpcc.5b04339 (2015).
45. Senlik, S. S., Policht, V. R. & Ogilvie, J. P. Two-color nonlinear spectroscopy for the rapid acquisition of coherent dynamics. *J. Phys. Chem. Lett.* **6**, 2413–2420, doi:10.1021/acs.jpcclett.5b00861 (2015).
46. Wells, K. L., Zhang, Z., Rouxel, J. R. & Tan, H.-S. Measuring the spectral diffusion of chlorophyll *a* using two-dimensional electronic spectroscopy. *J. Phys. Chem. B* **117**, 2294–2299, doi:10.1021/jp310154y (2013).
47. Irgen-Giorgio, S., Spencer, A. P., Hutson, W. O. & Harel, E. Coherences of bacteriochlorophyll *a* uncovered using 3D-electronic spectroscopy. *J. Phys. Chem. Lett.* **9**, 6077–6081, doi:10.1021/acs.jpcclett.8b02217 (2018).
48. Policht, V. R., Niedringhaus, A. & Ogilvie, J. P. Characterization of vibrational coherence in monomeric bacteriochlorophyll *a* by two-dimensional electronic spectroscopy. *J. Phys. Chem. Lett.* **9**, 6631–6637, doi:10.1021/acs.jpcclett.8b02691 (2018).
49. Meneghin, E., Pedron, D. & Collini, E. Characterization of the coherent dynamics of bacteriochlorophyll *a* in solution. *Chem. Phys.* **519**, 85–91, doi:https://doi.org/10.1016/j.chemphys.2018.12.008 (2019).
50. Policht, V. R. *et al.* Hidden vibronic and excitonic structure and vibronic coherence transfer in the bacterial reaction center. *Sci. Adv.* **8**, eabk0953, doi:doi:10.1126/sciadv.abk0953 (2022).
51. Fransted, K. A., Caram, J. R., Hayes, D. & Engel, G. S. Two-dimensional electronic spectroscopy of bacteriochlorophyll *a* in solution: Elucidating the coherence dynamics of the Fenna-Matthews-Olson complex using its chromophore as a control. *J. Chem. Phys.* **137**, 125101, doi:10.1063/1.4752107 (2012).
52. Fuller, F. D., Wilcox, D. E. & Ogilvie, J. P. Pulse shaping based two-dimensional electronic spectroscopy in a background free geometry. *Opt. Express* **22**, 1018–1027, doi:10.1364/oe.22.001018 (2014).
53. Rätsep, M., Linnanto, J. & Freiberg, A. Mirror symmetry and vibrational structure in optical spectra of chlorophyll *a*. *J. Chem. Phys.* **130**, 194501 (2009).
54. Picorel, R., Alfonso, M. & Seibert, M. in *Photosynthesis Research Protocols* (ed Robert Carpentier) 105–112 (Humana Press, 2011).

Figures

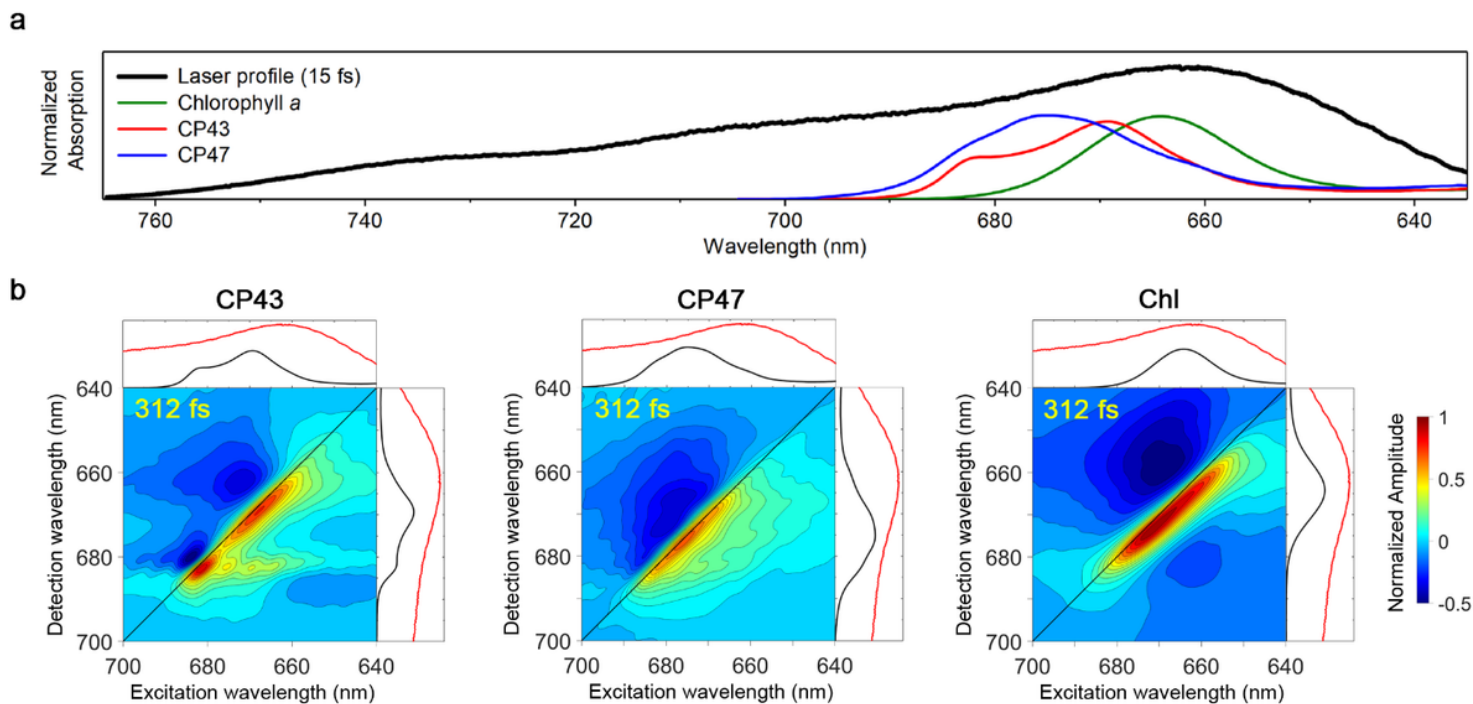


Figure 1

Spectroscopic data for CP43, CP47 and monomeric Chl at 77 K. (a) Linear absorption spectra of CP43 and CP47 normalized to the Chl content (13 Chls for CP43, 16 Chls for CP47) and Chl at 77 K (the Chl spectrum has been arbitrarily normalized to 13 Chls to ease comparison with CP43/CP47) together with the laser spectral profile utilized in the 2DES experiments (note that for collecting the Chl 2DES dataset the laser profile was shifted 10 nm to the blue in order to better excite and detect the Chl absorption bands). (b) 77 K real rephasing 2D spectra of CP43 (*middle*), CP47 (*left*) and Chl (*right*) at $T = 312$ fs. The spectra have been normalized to the peak amplitude at $T = 104$ fs (population time at which there is no contribution from the coherent artefact present around $T = 0$ fs). The linear absorption spectrum and the laser profile are shown at the top and right side of the 2D spectra to facilitate the assignment of the 2D spectral features to the linear absorption bands.

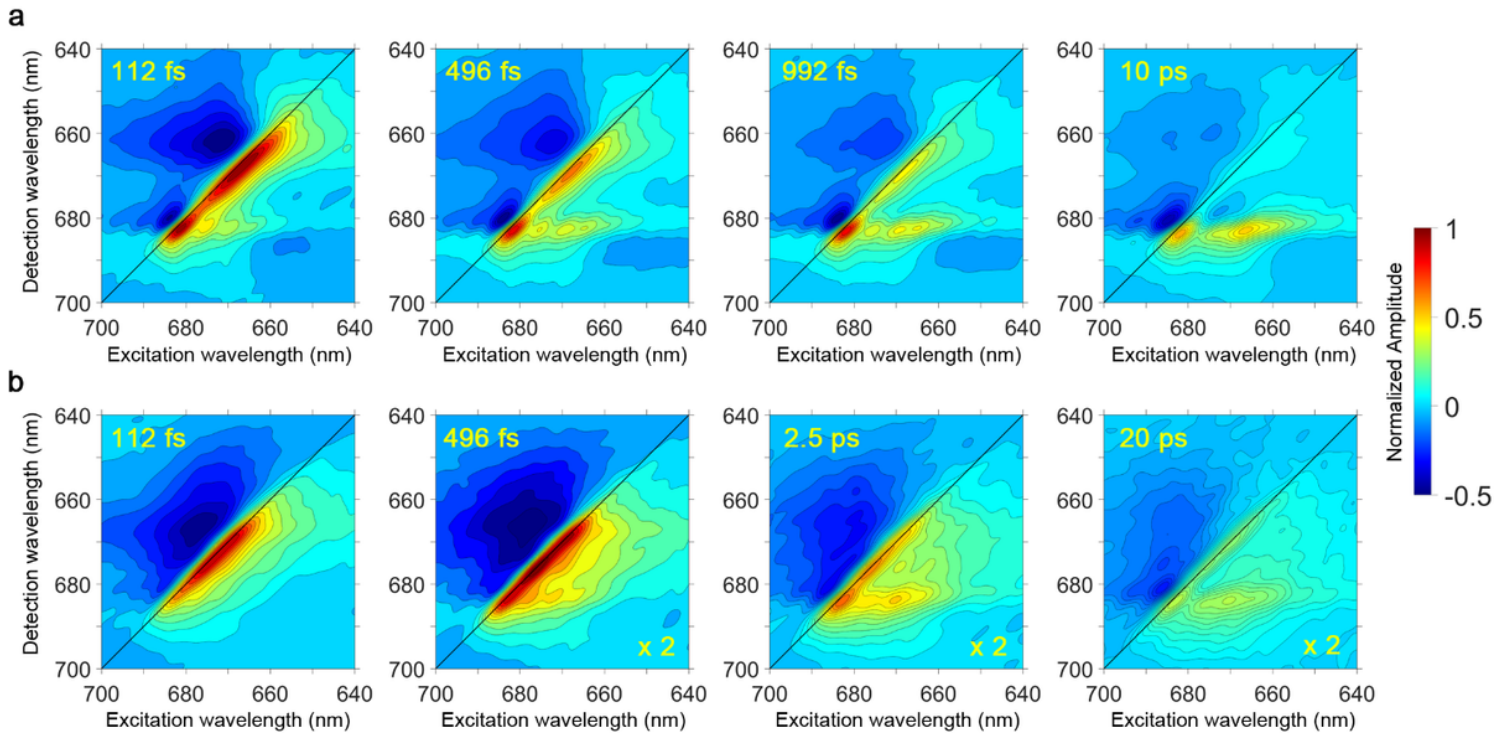


Figure 2

Real rephasing 2D spectra for CP43 and CP47 at 77 K for representative population times T . (a) CP43 real rephasing 2D spectra at 112 fs, 496 fs, 1 ps, and 10 ps. (b) CP47 real rephasing 2D spectra at 112 fs, 496 fs, 2.5 ps, and 20 ps. Due to the fast decay of the excited states and to facilitate the visualization of the spectral features; the 496 fs, 2.5 and 20 ps 2D spectra has been multiplied by 2. It is worth noting that the change in scaling does not modify the zero-value color of the displayed spectra. The 2D spectra has been normalized to the peak amplitude at $T = 104$ fs (population time at which there is no contribution from the coherent artefact).

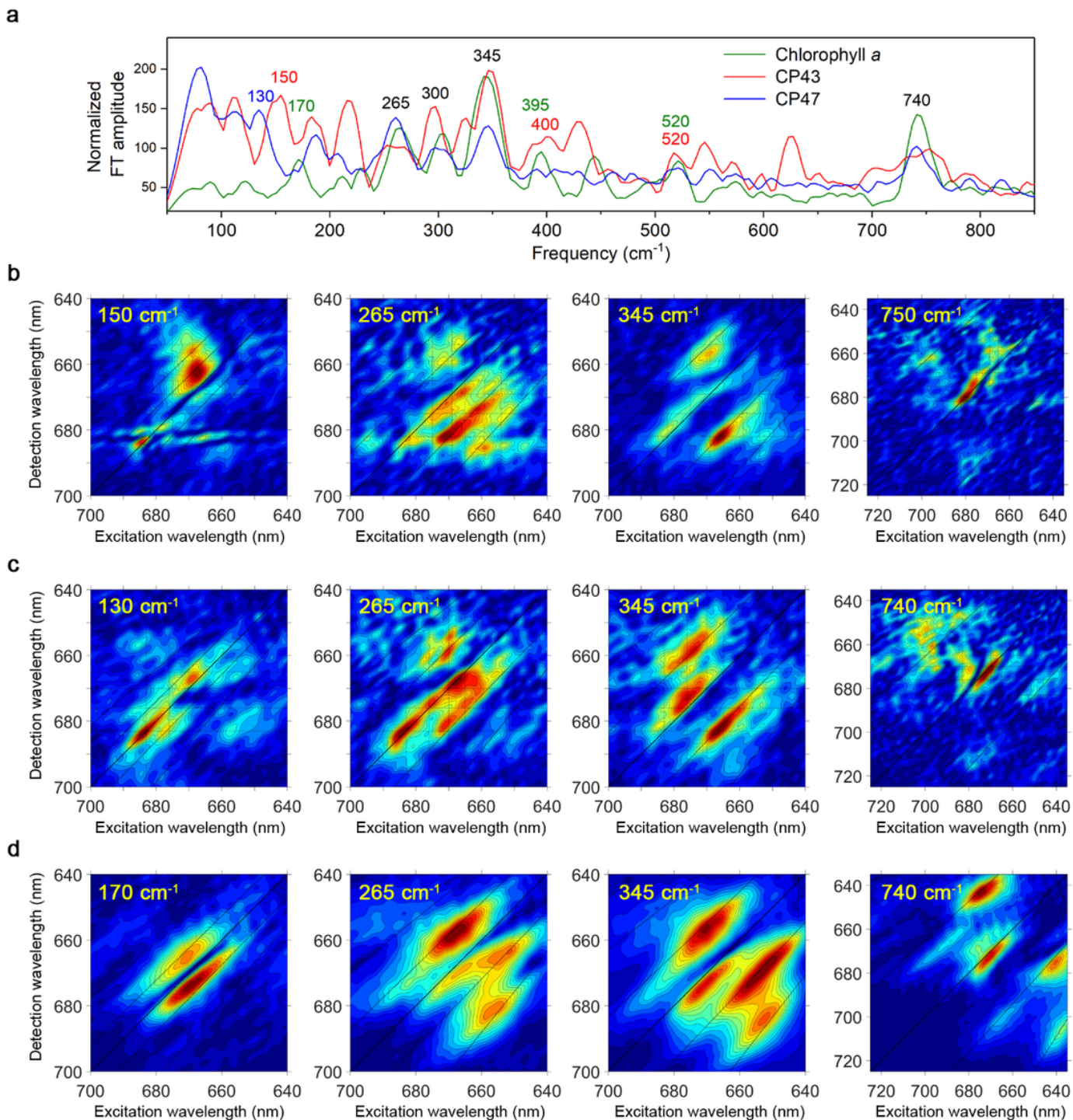


Figure 3

Oscillation frequencies and real rephasing 2D frequency maps for CP43, CP47 and monomeric Chl at 77 K. (a) Fourier transform (FT) of the real rephasing 2D spectral traces where the maximum amplitude value of each frequency across the full 2D spectra dataset is displayed. The FT is performed over a population time window 104 – 1504 fs (frequency resolution $\pm 20 \text{ cm}^{-1}$) with a step of 8 fs (maximum probed frequency $\approx 2100 \text{ cm}^{-1}$). Note that the monomeric Chl data has been divided by a factor of two to facilitate the comparison among the three datasets. (b) Real rephasing 2D frequency maps for CP43 at 150, 265, 345, and 750 cm^{-1} oscillation frequencies. (c) Real rephasing 2D frequency maps for CP47 at 130, 265, 345, and 740 cm^{-1} oscillation

frequencies. (d) Real rephasing 2D frequency maps for monomeric Chl at 170, 265, 345, and 740 cm^{-1} oscillation frequencies.

Supplementary Files

This is a list of supplementary files associated with this preprint. Click to download.

- [SupplementaryInformationCP43CP47NatComm.docx](#)